



**HAL**  
open science

## Macroscopic Versus Microscopic Schottky Barrier Determination at (Au/Pt)/Ge(100): Interfacial Local Modulation

Andrea Gerbi, Renato Buzio, César Gonzalez, Nicola Manca, Daniele Marre, Sergio Marras, Mirko Prato, Lloyd Bell, Sergio Di Matteo, Fernando Flores, et al.

### ► To cite this version:

Andrea Gerbi, Renato Buzio, César Gonzalez, Nicola Manca, Daniele Marre, et al.. Macroscopic Versus Microscopic Schottky Barrier Determination at (Au/Pt)/Ge(100): Interfacial Local Modulation. ACS Applied Materials & Interfaces, 2020, 12 (25), pp.28894-28902. 10.1021/acsami.0c07252 . hal-02928291

**HAL Id: hal-02928291**

**<https://hal.science/hal-02928291>**

Submitted on 9 Sep 2020

**HAL** is a multi-disciplinary open access archive for the deposit and dissemination of scientific research documents, whether they are published or not. The documents may come from teaching and research institutions in France or abroad, or from public or private research centers.

L'archive ouverte pluridisciplinaire **HAL**, est destinée au dépôt et à la diffusion de documents scientifiques de niveau recherche, publiés ou non, émanant des établissements d'enseignement et de recherche français ou étrangers, des laboratoires publics ou privés.

# Macroscopic vs Microscopic Schottky Barrier determination at (Au/Pt)/Ge (100): Interfacial Local Modulation

Andrea Gerbi,<sup>\*,†</sup> Renato Buzio,<sup>†</sup> Cesar González,<sup>‡</sup> Nicola Manca,<sup>†,#</sup> Daniele  
Marrè,<sup>†,#</sup> Sergio Marras,<sup>¶</sup> Mirko Prato,<sup>¶</sup>

Lloyd Bell,<sup>§</sup> Sergio Di Matteo,<sup>||</sup> Fernando Flores,<sup>‡</sup> and Pedro L. de Andres<sup>⊥</sup>

<sup>†</sup>*CNR-SPIN Institute for Superconductors, Innovative Materials and Devices,  
Corso Perrone 24, I-16152 Genova, Italy*

<sup>‡</sup>*Física Teórica de la Materia Condensada-IFIMAC,  
Universidad Autónoma de Madrid, E-28049 Madrid, Spain*

<sup>¶</sup>*Materials Characterization Facility, Istituto Italiano di Tecnologia, Via Morego 30,  
I-16163 Genova, Italy*

<sup>§</sup>*Jet Propulsion Laboratory, California Institute of Technology,  
4800 Oak Grove Dr. Pasadena, CA 91104, USA*

<sup>||</sup>*Univ. Rennes, CNRS, IPR (Institut de Physique de Rennes) - UMR 6251,  
F-35000 Rennes, France*

<sup>⊥</sup>*Instituto de Ciencia de Materiales de Madrid-CSIC, Cantoblanco,  
E-28049 Madrid, Spain*

<sup>#</sup>*Dipartimento di Fisica, Università degli Studi di Genova, via Dodecaneso 33,  
Genova, Italy*

E-mail: andrea.gerbi@spin.cnr.it

## Abstract

Macroscopic current-voltage measurements and nanoscopic Ballistic Electron Emission Spectroscopy (BEES) have been used to probe the Schottky barrier height at metal/Ge(100) junctions for two metal electrodes (Au, Pt) and different metallization methods; specifically, thermal-vapour and laser-vapour deposition. Analysis of macroscopic current-voltage characteristics indicates that a Schottky barrier height of 0.61-0.63 eV controls rectification at room temperature. On the other hand, BEES measured at 80 K reveals the coexistence of two distinct barriers at the nanoscale, taking values in the ranges 0.61-0.64 eV and 0.70-0.74 eV for the cases studied. For each metal/semiconductor junction, the macroscopic measurement agrees well with the lower barrier found with BEES. Ab-initio modelling of BEES spectra ascribes the two barriers to two different atomic registries between the metals and the Ge(100) surface, a significant relevant insight for next-generation highly miniaturized Ge-based devices.

## Keywords

Ballistic transport. Schottky barrier. Ballistic Electron Emission Spectroscopy. Green's functions methods. Density Functional Theory. Gold (Au). Platinum (Pt). Germanium (Ge).

## 1 Introduction

Germanium (Ge) has gained considerable attention as an alternative channel material for high-speed metal-oxide-semiconductor devices, due to its higher electron and hole mobilities relative to Si.<sup>1-5</sup> Moreover, Ge offers other advantages compared to Si, such as lower electronic bandgap (reducing the operating voltage for devices), a lower processing temperature (which is more suitable for integration with high k-dielectric materials) and higher saturation velocity (which can eliminate the problem of drain current saturation in MOS-

1  
2  
3 FETs). On the other hand, the electrically active defects at the Ge surface,<sup>6</sup> the larger defect  
4 densities at Ge/insulator interfaces, the necessity for passivation before deposition of gate  
5 dielectric materials, and the strong Fermi Level Pinning (FLP) at the Charge Neutrality  
6 Level (CNL),<sup>7-12</sup> have so far often limited the performance in Ge n-channel MOSFET. In-  
7 terestingly enough, Ge has recently shown tremendous potential as an alternative substrate  
8 for graphene growth<sup>13-15</sup> due to its catalytic activity,<sup>16</sup> extremely low solubility of carbon,<sup>17</sup>  
9 and the availability of large Ge area on Si.<sup>18</sup> Finally, the graphene/Ge heterostructure has  
10 proven useful for many applications.<sup>19-23</sup>

11  
12  
13 To boost technological developments, the nanoscale properties of Ge-based Schottky junc-  
14 tions must be studied further,<sup>24</sup> since semiconductor-based technology is reaching the scale  
15 where size effects begin to be significant. The long-debated problem of FLP assumes greater  
16 importance in the case of Ge because the position of the Fermi level, close to the valence  
17 band edge of Ge, is known to induce a strong inversion layer. This situation leads to a  
18 high Schottky Barrier Height (SBH) at the metal-semiconductor (MS) interface almost in-  
19 dependent of the metal's work-function,<sup>11,25</sup> which inhibits the formation of low resistance  
20 contacts. The origin of the FLP is usually associated to (i) surface states arising from de-  
21 fects and/or unsatisfied dangling bonds at the MS interface, (ii) Induced Density of Interface  
22 States (IDIS),<sup>26,27</sup> or (iii) Disorder Induced Gap States (DIGS).<sup>28</sup> The correct description  
23 is still under discussion and demands further research, in particular a systematic study of  
24 different metal-semiconductor interfaces, which are plans for the future.

25  
26  
27 Experiments aiming to characterize and better understand such a complex scenario are  
28 thus crucial both from a fundamental and a practical point of view, particularly in what  
29 concerns the role played by the metal/germanium (M/Ge) interface itself. In this context,  
30 Ballistic Electron Emission Microscopy (BEEM) and the associated Spectroscopy (BEES) are  
31 powerful techniques capable of achieving nanoscale resolution of the electrostatics landscape  
32 at the MS interface. BEEM is an extension of Scanning Tunnelling Microscopy (STM)  
33 where a tip at bias  $V_T$  injects ballistic electrons into a thin metal overlayer at constant  
34  
35  
36  
37  
38  
39  
40  
41  
42  
43  
44  
45  
46  
47  
48  
49  
50  
51  
52  
53  
54  
55  
56  
57  
58  
59  
60

1  
2  
3 tunnelling current  $I_T$ . If the energy of the electrons overcomes the buried energy barrier  
4 formed between the metal and the underlying semiconducting substrate, a current  $I_B$  is  
5 transmitted across the sample and collected through the backside ohmic contact. The SBH  
6 is then defined by the onset of the collector current in  $I_B$  vs  $V_T$  spectra. BEES allows a  
7 nanometric determination of interfacial band bending, while probing the junction under a  
8 zero-bias condition without affecting the band structure, and with a high energy resolution  
9 of  $\approx 20$  meV at low temperature.<sup>29,30</sup>

10  
11 Despite a large number of studies concerning the characterization of metal/germanium  
12 SBH by macroscale techniques, a detailed microscopic study by BEES of such M/Ge interface  
13 is missing, even though studies have been published on buried Ge dots, and  $\text{Si}_{1-x}\text{Ge}_x$  strained  
14 interfaces.<sup>31,32</sup> In this paper, we characterize the SBH formed at the M/Ge(100) interface  
15 by analyzing BEES measurements in the framework of a recently developed N-order ab-  
16 initio modelling, which makes possible to treat large enough interfaces to explore more  
17 realistic models for the system.<sup>33</sup> Au/Ge(100) contacts have been prepared by depositing  
18 under Ultra High Vacuum (UHV) a Au electrode of about 15 nm nominal thickness on  
19 atomically flat Ge(100)<sup>34-37</sup> by Physical Vapour Deposition (PVD), while another set of  
20 Schottky junctions were prepared on the same substrate by depositing either Au or Pt by  
21 Pulsed Laser Deposition (PLD). Microscopic BEES measurements were performed under  
22 UHV at  $T = 80$  K using a modified commercial STM apparatus, and macroscopic two-point  
23 Current-Voltage (I-V) measurements were acquired in situ at room temperature,  $T = 290$  K  
24 (RT), and at a lower temperature,  $T = 80$  K.

## 2 Experimental

### 2.1 Substrate preparation

25  
26  
27  
28  
29  
30  
31  
32  
33  
34  
35  
36  
37  
38  
39  
40  
41  
42  
43  
44  
45  
46  
47  
48  
49  
50  
51  
52  
53  
54  
55  
56  
57  
58  
59  
60  
Figure 1 shows a scheme for the experimental setup (upper panel) and the corresponding  
energy bands. The substrate used was Ge(100) (n-type, Sb-doped, 3.97-4.46  $\Omega$ -cm, 3.4-

1  
2  
3  $4 \times 10^{14} \text{ cm}^{-3}$ , MTI Corporation). To prepare the junctions between the substrate and high  
4 work-function metals (namely, Pt and Au), we cut the Ge substrate into pieces of about  
5  $10 \times 5 \times 0.5 \text{ mm}^3$  and cleaned them in ultrasonic baths of acetone (5 min) and 2-propanol  
6 (5 min), followed by drying in pure  $\text{N}_2$  flow. In order to remove the native oxide, the pieces  
7 were placed in a bath of hot deionized water (85 °C) for 5 min and then dipped in a 5%  
8 aqueous HF solution, which was followed by a further immersion in deionized water at room  
9 temperature to block the acidic attack. Finally, they were dried in pure  $\text{N}_2$  flow. The use of  
10 HF is known to produce a hydrogen-terminated surface for Ge(100).<sup>34</sup> Hydride-terminated  
11 Ge shows no oxidation after exposure to ambient atmosphere for at least one hour<sup>35-37</sup> and  
12 little oxidation after one week.<sup>36</sup> Accordingly, the pieces were loaded within few minutes into  
13 UHV deposition chambers for the Schottky junction preparation.  
14  
15  
16  
17  
18  
19  
20  
21  
22  
23  
24  
25  
26

## 27 2.2 Schottky Junction and Ohmic contact preparation

28  
29 The Au/Ge(100) contacts were prepared by depositing under UHV condition Au electrodes  
30 of about 15 nm nominal thickness on Ge(100) by PVD, base pressure below  $10^{-8}$  mbar,  
31 deposition rate of about 1.5 nm/min, through a shadow mask (area of  $A = 2.3 \pm 0.1 \text{ mm}^2$ ).  
32 Another set of Schottky junctions were prepared on the same substrate but by depositing  
33 both Au and Pt by PLD, target-substrate distance 5 cm, area  $2.3 \text{ mm}^2$ , base pressure  $10^{-7}$   
34 mbar, deposition rate 3 Hz, nominal thickness 12-15 nm for Pt/Ge(100) (Pt PLD) and 13-16  
35 nm for Au/Ge(100) (Au PLD). Au and Pt grounding are prepared by gently touching a thin  
36 wire on a small drop of silver paste deposited on the metal surface and then dried below a  
37 light (see the scheme in the upper panel of Figure 1).  
38  
39  
40  
41  
42  
43  
44  
45  
46

47 In all cases, the Ge(100) ohmic back-contact was obtained by depositing a thick Al film by  
48 PLD from high-purity target (thickness  $\approx 100 \text{ nm}$ ) on the back side of the substrate (target-  
49 substrate distance 5 cm, base pressure  $10^{-7}$  mbar, deposition rate 10-20 Hz (deposition time  
50 30-40min).  
51  
52  
53  
54  
55  
56  
57  
58  
59  
60

## 2.3 BEES and macroscopic I-V apparatus

BEEM was performed under UHV using a modified commercial STM (LT-STM by Omicron Nanotechnology GmbH, Germany) with a base pressure of  $3 \times 10^{-10}$  mbar equipped with an additional low-noise variable-gain current amplifier (custom DLPCA-200 by FEMTO GmbH, Germany). The sample was mounted on a specially designed BEEM plate to ensure proper electrical grounding, allowing independent measurement of both  $I_T$  and  $I_B$ . Two-point I-V measurements were acquired in-situ using a Keithley (Model 6430 Sub-Femtoamp Remote Source-Meter) source measurement unit at RT and at 80 K to ensure rectification (voltage sweeping 2 s per 10 mV step). All measurements were taken under dark condition in order to reduce the photocurrent contribution (see the scheme in the lower panel of Figure 1).

The sample was loaded into the UHV chamber within one hour from the deposition and immediately cooled down to 80 K for BEEM studies; all BEES spectra were acquired at 80 K. Data at each bias voltage were obtained by averaging 4096 samples. A typical experiment consisted of 1600-3600 spectra acquired on a regular grid ( $40 \times 40$  up to  $60 \times 60$ ) at different metal surface spots in order to reduce electron beam damage (average separation between two adjacent curves is 10 nm). Each curve was acquired in 6 s. Noise current fluctuations in individual raw spectra amounted to about 5fA peak to peak at the temperature of  $T = 80$  K. Many different spectra were acquired on different macroscopic locations of the sample in order to verify the reproducibility of the SBH distribution. We have also performed measurements at different injected currents in the range from 20 pA to 5 nA. Typically, the image lateral size was from  $300 \times 300 \text{ nm}^2$  up to  $1000 \times 1000 \text{ nm}^2$ . Unless otherwise specified, the STM tip (gold, mechanically cut at a steep angle) was negatively biased with respect to ground, meaning that the electron transport occurs from the STM tip to the metal and semiconductor. For the acquisition of each BEES spectrum, the tip voltage  $V_T$  was ramped under feedback control while keeping the tunnelling current constant.

### 3 Modelling

#### 3.1 Macroscopic Thermoionic Theory

The macroscopic I-V data have been analyzed according to the equivalent-circuit based on a diode with a parasitic leakage due to a parallel conductance ( $G_p$ ) and a resistor in series ( $R_s$ ). This model provides a voltage current relationship given by<sup>24,38</sup>

$$I(V, T) = I_d + I_p = I_S \left( e^{\frac{V - IR_S}{nk_B T}} - 1 \right) + G_p (V - IR_S), \quad (1)$$

where  $n$  is the ideality factor. The saturation current  $I_S$  in the thermionic emission approximation is given by

$$I_S = SA^*T^2 e^{-\frac{q\Phi}{k_B T}}, \quad (2)$$

where  $S$  is the diode area ( $2.3 \text{ mm}^2$ ), and  $A^*$  the Richardson's constant ( $140 \text{ A cm}^{-2} \text{ K}^{-2}$ ). The effective Schottky barrier height ( $\Phi$ ) the ideality factor ( $n$ ) the series resistance ( $R_s$ ) and the parallel conductance ( $G_p$ ) were treated as free parameters and were estimated from best-fits to experimental curves.

#### 3.2 Microscopic ab-initio Phase-Space Theory

Best fits to BEES spectra have been obtained using the ab-initio ballistic phase-space model<sup>33</sup>

$$I_B(V_T, T) = I_0 + \alpha \int_0^\infty \frac{E^{\mu-1} dE}{e^{\frac{E + \Phi - V_T}{k_B T}} + 1} = I_0 - (k_B T)^\mu \alpha \Gamma[\mu] \text{Li}_\mu \left( -e^{\frac{V_T - \Phi}{k_B T}} \right), \quad (3)$$

where  $\Gamma$  is the Legendre's Gamma function,  $\text{Li}$  is the Jonquière's function,<sup>39</sup>  $I_0$  is a constant representing the small fluctuating value for the current in the region below the local Schottky barrier  $\Phi$  ( $I_0 \approx 2 - 5 \times 10^{-6}$ , normalized to  $I_T$ ),  $V_T$  is the tip voltage,  $T$  is the temperature and,  $\alpha$  is a scale factor such that  $I(V_T = \Phi)$  coincides with the experimental value.



Previous attempts to determine a simple expression for BEES spectra that may allow for a quick determination of the Schottky barrier date back to the pioneering work by Bell and Kaiser<sup>40</sup> and their proposal to consider an energy-independent transmission coefficient at the interface, resulting in the direct expression  $I(V_T) = \alpha V_T^2$ , i.e.  $\mu = 2$ . Such a law has become a *de facto* standard in the field due to its general good agreement with experiments and its simplicity of use. Other authors, however, have pointed out that some dependence with energy for the transmission coefficient is to be expected; the simplest alternative model being proposed by Prietsch and Ludeke resulting in  $\mu = 2.5$ .<sup>41</sup> Attempts to incorporate a variety of effects have resulted in  $\mu$  taking values between 1 and 3.5, which translates in an uncertainty of fitted values for the Schottly barrier of about 0.1 eV.<sup>42</sup> Therefore, it is of paramount importance to determine a precise value for  $\mu$  in order to claim good accuracy in the determination of the onset.

To get a first-principles value for  $\mu$ , independent of simplifying hypotheses, we utilize a localized-basis ab-initio DFT approach<sup>43</sup> that allows us to write the total hamiltonian for the tip, metal base, and semiconductor, in a second-quantization formalism:

$$H = \sum_{\alpha} \epsilon_{\alpha} n_{\alpha} + \sum_m \epsilon_m n_m + \sum_{m,m'} T_{mm'} c_m^{\dagger} c_{m'} + \sum_s \epsilon_s n_s + \sum_{s,s'} T_{ss'} c_s^{\dagger} c_{s'} + \sum_{\alpha,m} T_{\alpha m} c_{\alpha}^{\dagger} c_m + \sum_{m,s} T_{ms} c_m^{\dagger} c_s \quad (4)$$

where  $\alpha$  refer to sites in the tip;  $m, m', \dots$  to the metal base; and  $s, s', \dots$  to the semiconductor substrate. Interaction terms are given by hopping matrices between the metal and the semiconductor,  $T_{ms}$ , and the tip and the base metal,  $T_{\alpha m}$ ; in a typical tunneling regime this is assumed to be small and approximated only by the interaction between the last tip atom and the few closest metal atoms.

The BEES current injected into the semiconductor can thus be obtained from the Green's functions  $G$  related to hamiltonians in Equation (4) for the tip, metal slab, and semi-infinite semiconductor, considered as non-interacting systems,

$$I_B(V_T) = \frac{4e}{\hbar} \int_{\Phi}^{V_T} \frac{dE}{2\pi} \int_{\text{IBZ}} d^2\vec{k}_{\parallel} \sum_{(m,m') < s} \text{Tr} [\mathcal{D}_{m,1}^R \Gamma_{1,1'} \mathcal{D}_{1',m'}^A \Gamma_{m',m}] \quad (5)$$

where  $\Gamma_{m',m} = T_{m',s} \rho_{s,s'}^{(S)} T_{s',m}$  and  $\Gamma_{1,1} = T_{1,0} \rho_{0,0}^{(T)} t_{0,1}$  are injection rate matrices involving the metal-semiconductor interface and the tip-metal gap,<sup>44</sup> and  $\rho_{ll'}^{R,A} = \mp i\pi \text{Im} G_{ll'}^{R,A}$  is the retarded (R) or advanced (A) density of states on the tip (T) or the semiconductor (S). The renormalized multiple-scattering Greens functions  $\mathcal{D}$  are computed from Green's functions  $G$  related to the isolated components of the system,

$$\begin{cases} \mathcal{D}_{m,1}^R = \left( \delta_{m,m''} - G_{m,s}^R T_{s,s'}^{(S)} G_{s',s''}^R T_{s'',m''}^{(S)} \right)^{-1} G_{m'',1}^R \\ \mathcal{D}_{1,m}^A = G_{1,m''}^A \left( \delta_{m'',m} - T_{m'',s}^{(S)} G_{s,s'}^A T_{s',m'}^{(S)} G_{m',m}^A \right)^{-1} \end{cases}$$

Using this formalism, it is possible to compute Green's functions of order  $N + 1$  starting from uncoupled Green's functions of order  $N$ , therefore making the calculation an efficient  $N$ -order procedure that allows to tackle thick layers, while still solving the problem from first-principles.<sup>45</sup>

A best-fit of Equation 5 to Equation 3 determines a parameter-free value for  $\mu$ , which is found to depend mostly on the metal-semiconductor combination. To get a consistent value for  $\mu$  it is necessary to restrict the fitting procedure to an interval where the main hypotheses behind Equation 3 apply; namely, (i) only a single minimum in the conduction band adds to the current (other minima are expected to work as new channels with the same value of  $\mu$ ) and, (ii) since we are only interested in the ballistic current, the contribution of secondary electrons to BEEM current should not be significant. In Section 4.3 we explain in detail why the interval  $(\Phi, \Phi + 0.15)$  eV is adequate regarding the electronic bandstructure of Ge. Relevant to the second condition, the mean free path of BEEM carriers decays as  $\propto \frac{1}{\sqrt{2}}$ . For Au, we have determined  $\lambda \approx 1500 - 1000 \text{ \AA}$  in the interval used in the fits, while for Pt we estimate that it takes a value about  $300 \text{ \AA}$ .<sup>46</sup> Therefore, the width of the metal base,  $w \approx 150 \text{ \AA}$  is always smaller than the mean free path of carriers and the likelihood of inelastic

1  
2  
3 events is small. Finally, Monte-Carlo simulations show that secondary electrons pick up, on  
4  
5 average, about half of the energy of primary carriers, which again is a safe condition as long  
6  
7 as  $\Phi + \Delta \leq \Phi$ .<sup>47</sup> In summary, working within such interval, we obtain for Au/Ge  $\mu = 2.11$   
8  
9 and, for Pt/Ge  $\mu = 2.01$ , cf. Section S6.1 in Supporting Information.

10  
11 These two values are close enough to 2 to justify, at least for the two junctions studied  
12  
13 here, the widespread surprising assumption of a nearly constant transmission coefficient at  
14  
15 the interface.<sup>48</sup> In addition, we notice that a precise determination for the onset requires  
16  
17 to incorporate thermal effects because these can affect its position by  $\approx 0.02$  eV at  $T = 80$   
18  
19 K. Finally, the interface has been modelled as a set of parallel conduction channels each  
20  
21 described by Equation (3) with its own characteristics parameters. For cases where a best fit  
22  
23 to experiments demands two or more barriers, a superposition of currents has been used, as  
24  
25 described individually for each Schottky barrier in Equation (3). To give similar importance  
26  
27 to high and low intensities in the fit process, we work with  $\log_{10} I$  rather than directly with  $I$ .  
28  
29 We point out that in Equation (3) only two parameters are free to be fitted to experiments:  
30  
31  $\Phi$  and  $\alpha$  (see Table 1) and, although possible in principle, the correlation between them is  
32  
33 small because of the way  $\alpha$  has been defined.

## 34 35 36 37 **4 Results and discussion**

### 38 39 40 41 **4.1 Macroscopic Junctions**

42  
43 The evolution of the macroscopic junctions in response to different metallization meth-  
44  
45 ods has been characterized by interpolating the forward bias region of I-V curves with the  
46  
47 Thermionic-Emission theory (TE).<sup>38</sup> Representative I-V characteristics acquired at 290 K  
48  
49 are given in Figure 2. They show current rectification with polarity consistent with n type  
50  
51 carriers type, and rectification ratios of about 10-60 at  $\pm 0.2$  V. It is worth to notice that the  
52  
53 PLD high-energy deposition process does not modify the response of the Au/Ge interface  
54  
55 compared to its PVD version. Additionally, if we consider the intensity of the reverse bias  
56  
57  
58  
59  
60

1  
2  
3 current, we observe a reduction for PLD-deposited Pt that gives a leakage comparable to  
4 that obtained by e-beam deposited Pt.<sup>6</sup> Our Pt<sub>PLD</sub>/Ge interface shows lower leakage current  
5 ( $10^{-5}$  A) in the reverse bias region, whereas comparable current values are found for contacts  
6 prepared with Au<sub>PVD</sub> and Au<sub>PLD</sub>.  
7  
8  
9

10  
11 We have obtained nearly ideal Schottky diodes for Au<sub>PVD</sub> and Au<sub>PLD</sub>, with ideality  
12 factor  $n \approx 1$ , and SBH values in good agreement with previous reports.<sup>1</sup> The slight increase  
13 of  $n = 1.14$  for Pt<sub>PLD</sub>, is comparable to values previously reported for the Pt/Ge interface.<sup>6</sup>  
14 Therefore, the similarity of  $n$  values for Au<sub>PVD</sub> with those of Au<sub>PLD</sub>, and their closeness  
15 to 1 confirm the reduced damage effect produced by the PLD deposition. The SBH values  
16 extracted from I-V curves are very similar too, regardless of the metal deposition technique  
17 and the work function. Furthermore, they are slightly smaller than the Ge bandgap (0.66  
18 eV at RT), thus supporting the existence of strong FLP near the valence band.  
19  
20  
21  
22  
23  
24  
25  
26  
27  
28

## 29 4.2 Microscopic Junctions

30  
31 In addition, we have investigated SBH values at the nanoscale by performing BEES on  
32 different positions of the M/Ge(100) interface at low temperature,  $T = 80$  K, since at  
33  $T = 290$  K the junction zero-bias current noise dominates the BEES spectra, making them  
34 not informative. Figure 3 shows a typical topography and the related BEEM current map  
35 for Au<sub>PVD</sub>/Ge(100), acquired over a representative region of the Au electrode. Topography  
36 reveals a granular structure of 10-30 nm in diameter, and the surface height range (2nm  
37 peak-to-peak) is smaller than the Au nominal thickness. We observe that the associated  
38 BEEM map is influenced by the surface morphology, as the spatial variations of ballistic  
39 current  $I_B$  localize at grains boundaries. The current amplitude, however, does not change  
40 systematically with the local surface slope or the thickness of the Au film; BEEM contrast  
41 mostly reflects contributions from the polycrystalline nature of the Au film.  
42  
43  
44  
45  
46  
47  
48  
49  
50  
51  
52

53 Results for representative BEES spectra, each obtained from the average of 1600 BEES  
54 measurements performed on a grid pattern in a  $600 \times 600$  nm<sup>2</sup> surface, are shown on Figure 5  
55  
56  
57  
58

1  
2  
3 for the three types of devices. Best fits (black lines) have been obtained using the ab-  
4 initio ballistic phase-space model, Equation (3); all of them are of excellent quality just by  
5 visual inspection, both for the function (the target) and the first derivative (cf. insets), we  
6 point out that the excellent agreement in the derivative is entirely due to the agreement  
7 achieved for the function since the fitting procedure does not use values of the derivative.)  
8 To further quantify the agreement, we have computed a figure of merit,  $R$ , that compares  
9 the absolute difference of decimal logarithms between experimental and modeled intensities  
10 (hence weighting similarly low and high-intensity regions). Values given in Table 1 for these  
11 R-factors corroborate the good correlation between experimental data and model fits yielding  
12 values for the SBH. We remark that, since the fit to  $\mu$  has been obtained in the interval  
13  $(\Phi, \Phi + 0.15)$ , curves outside that region should be taken as an extrapolation, although a  
14 reasonable one. Curves in Fig. 5 haven been drawn up to  $\approx 0.2$  eV only for the sake of  
15 clarity.  
16  
17  
18  
19  
20  
21  
22  
23  
24  
25  
26  
27  
28

29 Our ab-initio phase-space ballistic model shows the appearance of a double barrier in both  
30 the Au<sub>PVD/PLD</sub>/Ge and Pt<sub>PLD</sub>/Ge devices. A telltale for the existence of a second onset can  
31 be deduced immediately from the change in the slope in the Log-Log plot. Since the Log-Log  
32 of  $I \propto (V - \Phi)^\mu$  is a straight line, provided that the origin is chosen so  $\Phi = 0$  and  $I_0 = 0$ , this  
33 is a useful representation to identify the quasi-linear behaviour on such representation. The  
34 abrupt change in the slope w.r.t such a linear reference marks the appearance of a second  
35 onset, which is independently corroborated by looking at the derivative of the intensity.  
36 The power law is so close to  $V^2$  that a straight line represents the first derivative well  
37 and, the appearance of a second onset determines an easily identifiable abrupt change in  
38 the slope of the derivative (behaviour seen around  $\approx 0.7$  eV in the insets in Figure 5, red  
39 lines). In addition, Figure 6 shows normal-like probability distributions and  $\Phi_i$  histograms  
40 obtained by applying to a set of individual normalized BEES  $I(V)$  curves a Levenberg-  
41 Marquardt algorithm and Bell-Kaiser's model,<sup>29</sup>  $\alpha V^\mu$ , which corresponds to the ab-initio  
42 phase-space equation<sup>33</sup> for  $T = 0$  K and  $\mu = 2$  (an approximation that considerably simplifies  
43  
44  
45  
46  
47  
48  
49  
50  
51  
52  
53  
54  
55  
56  
57  
58  
59  
60

1  
2  
3 the Levenberg-Marquardt's non-linear optimization to get individual  $\Phi_i$  for each measured  
4 spectra). A comparison with a full optimization based in the full expression, Equation (3),  
5 which takes into account the temperature and the value for  $\mu$  corresponding to each metal-  
6 semiconductor junction, shows corrections in the determination of the Schottky barrier of  
7 about 10 to 20 meV. These offsets, when applied to the calculated histograms tend to make  
8 the average value of the distribution of individual experiments to coincide with the ensemble  
9 average value, as it is shown in Figure 6. For Au<sub>PLD</sub>/Ge, 1600 different locations on the same  
10 sample have  $\Phi_1 = 0.64 \pm 0.01$  eV and  $\Phi_2 = 0.71 \pm 0.01$  eV. For Pt<sub>PLD</sub>/Ge, 1600 different  
11 locations on the same sample have  $\Phi_1 = 0.63 \pm 0.01$  eV and  $\Phi_2 = 0.74 \pm 0.02$  eV. The  
12 statistical spread of the histogram originates from three distinct contributions: (i) spatial  
13 variations of the barrier height at the buried interface, (ii) noise (including also the tunnelling  
14 current noise), and (iii) broadening due to thermal noise. Careful analysis indicates that  
15 experimental uncertainty contributes to the spread with 3-5 meV at 80 K; therefore, the  
16 actual barrier inhomogeneity at the M/Ge(100) interface is substantially unaffected by the  
17 instrumental noise. In this respect, it is known that the poly-crystallinity of the metal  
18 electrode, impurities, dopants, oxide traces and defects at the interface are by themselves  
19 sufficient to explain such large fluctuations.<sup>24</sup>

### 4.3 Physical Origin of the Second Onset

40  
41 To discuss the physics behind a second onset we examine (i) the contribution from secondary  
42 band-structure minima in the semiconductor,<sup>40</sup> and (ii) structural effects at the interface.  
43 Indeed, accurate analysis of the Schottky barrier needs to take into account on a similar  
44 footing electronic and geometrical effects and their mutual interplay.

45 For Au/Ge we have unequivocally identified the contribution of a second threshold at  
46  $\Phi_2 = \Phi_1 + 0.095$  eV (PVD) and,  $\Phi_2 = \Phi_1 + 0.073$  eV (PLD), cf. Table 1. Regarding the  
47 role of band-structure effects, low-temperature measurements on Ge by Magneto-Absorption  
48 yield an indirect gap of  $0.744 \pm 0.001$  eV ( $L_{6c}^+$ ), followed by a direct gap of  $0.898 \pm 0.001$  eV

1  
2  
3  $(\Gamma_{6c}^-)$ .<sup>49</sup> Therefore, a second onset due to the first available local minimum in the conduction  
4 band cannot happen below  $\Delta_{\Gamma} = \Phi_2 - \Phi_1 = 0.154$  eV (0.15 eV at 80 K). The next local  
5 minimum is located near  $X_{5c}$  at  $\Delta_X \geq 0.25$  eV, which is quite far away for our purposes.  
6  
7 These values have been corroborated both by angle-resolved photoemission,<sup>50</sup> and theoretical  
8 calculations.<sup>51</sup> We conclude that the appearance of a second onset in Au/Ge with values  
9  $\Delta < 0.15$  eV due to injection of electrons in  $\Gamma$  can be discarded.  
10  
11  
12  
13  
14

15 Therefore, we turn our attention to structural effects. First, we have studied in great  
16 detail the interface between  $\sqrt{2} \times \sqrt{2}$  R45° Au(001) and  $1 \times 1$  Ge(001).<sup>33</sup> Such an interface  
17 presents the advantage of having minimal surface stress and of being also amenable to accu-  
18 rate and extensive calculations, since it is one of smallest possible 2D interfacial unit cells.  
19 Symmetry considerations show that metallic (001) planes have two possible registries w.r.t.  
20 Ge(001) with similar interfacial stress and total energy. In one of the registries, both Au  
21 atoms in the 2D unit cell are located on bridge sites (BB), while in the other registry the  
22 combination is atop and hollow (TH), cf. Fig. S11. One of these configurations naturally  
23 corresponds to a slightly lower total energy (here BB) and, it is preferred, but the existence of  
24 interfacial stress due to the lack of perfect agreement between the metal and semiconductor  
25 2D unit cells facilitates the mixture of both. We have found that the interfacial dipoles at  
26 the two interfaces result in a displacement of the corresponding Shottky barriers by  $\Delta = 0.1$   
27 eV (cf. Section S6.3), which is in agreement with the experimental values we have found. On  
28 the other hand, X-ray Diffraction (XRD) tell us about the abundance of Au(011) planes for  
29 Au/Ge (Section S2). Therefore, we have looked at the interface,  $1 \times 7$  Au(011)/ $1 \times 5$  Ge(001),  
30 cf. Fig. 4, which is among the simplest for this orientation compatible with a small interfacial  
31 stress. Again, two registries are manifestly possible by symmetry: (i) metal-semiconductor  
32 coordination via atop and quasi-bridges (T) and (ii) coordination via mostly bridges sites  
33 (B). We find a shift in the Shottky barriers corresponding to these registries of  $\Delta = 0.061$   
34 eV, which again is in good accordance with our experimental findings.  
35  
36  
37  
38  
39  
40  
41  
42  
43  
44  
45  
46  
47  
48  
49  
50  
51  
52  
53  
54

55 Pt/Ge makes a more complex case for several reasons. Experimentally, we have found  
56  
57  
58  
59  
60

1  
2  
3  $\Delta = +0.11$  eV, cf. Table 1. Here, XRD shows that the stacking of metallic (111) planes is  
4 a major component, cf. Section S2. Therefore, we have studied the simplest model for such  
5 interface having a minimal amount of interfacial stress,  $2 \times 7$  Pt(111) /  $1 \times 6$  R45° Ge(001),  
6 cf. Figure S12. The mixing of four-fold and three-fold symmetries makes it challenging  
7 to establish a definitive relationship between atoms across the interface and, consequently,  
8 a good deal of disorder is seen, making difficult to establish a good epitaxy. Such a con-  
9 clusion is in agreement with the XRD analysis. On the other hand, it is well-known that  
10 injected electrons propagate through (111) and (100) planes similarly, due to comparable  
11 bandgaps opening along these directions.<sup>47</sup> Such electronic effect in the propagation through  
12 the metallic base alters the available configuration space for carriers inside the semiconduc-  
13 tor due to  $\vec{k}_{\parallel}$  conservation, preventing injection of electrons in Ge near  $\Gamma_{6c}^-$ , and making  
14 even more unlikely the contribution of this secondary minimum. Therefore, this is a case  
15 where the atomic stacking of planes on the metal base critically modulates the available  
16 electronic states in the semiconductor. Taking into account the difficulties of modelling the  
17 Pt(111)/Ge(001) interface with the necessary detail, we restrict ourselves to a proof of con-  
18 cept on  $\sqrt{2} \times \sqrt{2}$  R45° Pt(001) / Ge(001), which can be argued to be a good model from  
19 the point of view of BEEM because of the aforementioned similarities between propagation  
20 through (001) and (111) planes. In line with our results for Au/Ge, we find  $\Delta = 0.05$  eV for  
21 the two possible registries, which again we consider a good indication of the prevalence of  
22 structural effects in the origin of a second onset near the first one for the case of Pt/Ge too.  
23  
24  
25  
26  
27  
28  
29  
30  
31  
32  
33  
34  
35  
36  
37  
38  
39  
40  
41  
42

43 Finally, we comment that from a theoretical point of view, ballistic electrons propagate  
44 forming diffraction lines in accordance with the electronic band structure in the metallic thin  
45 film.<sup>47,52</sup> For propagation perpendicular to (001) planes, these lines spread as a cone with  
46 semi-aperture of about 45°; i.e., for a base metal layer of width  $w \approx 100$  Å, these diffraction  
47 lines extend over regions of about 200 Å in size, which explains why BEES carries information  
48 about domains several hundreds of Å apart in spite of its nanometric resolution.  
49  
50  
51  
52  
53  
54  
55  
56  
57  
58  
59  
60



## 4.4 Conclusions

We have achieved efficient metal-semiconductor rectifying junctions by depositing Au and Pt on Ge(100) by PVD and PLD. The latter method has the advantage of being able to deposit different metals with different melting points in a simple way. The use of Ge as substrate for rectifying devices presents a few advantages; however, further research is still needed to exploit them fully. In particular, regarding the strong Fermi level pinning, which limits the performance in n-Ge based MOSFET. For the metal/semiconductor combinations considered in this work, a robust interfacial band bending and Fermi level pinning (independent from interfacial defects issues) has been found.

The ab-initio phase-space ballistic model has been used to analyze state-of-the-art UHV low-temperature BEES measurements on two metals (Au and Pt) deposited on Ge(001), allowing us to determine values for the Schottky barrier  $\Phi_1$  with unprecedented accuracy. We identify in all cases a second Schottky onset contributing to the BEES current, which appears near the first one,  $\Phi_2 - \Phi_1 \approx 0.1$  eV, and cannot be associated to injection near  $\Gamma$ , which would imply  $\Phi_2 - \Phi_1 \geq 0.15$  eV. An alternative explanation is proposed by analyzing atomistic models optimized with DFT for the interface. Configurations related by a 2D registry shift between metal and semiconductor planes, which have nearly the same interaction energy and interfacial stress, produce differences in the interface dipoles that can explain the value of such microscopic secondary onset. Furthermore, macroscopic I-V measurements performed at room temperature yield values for the Schottky barrier which match well with the lower barrier measured in the nanoscopic BEES experiment and, are quite insensitive to the two different deposition methods we have investigated (PVD and PLD). Full agreement with conventional I-V literature has been achieved, while at the same time new information has been raised by microscopic measurements (BEES), which yield a more accurate and more detailed picture for the Schottky barrier than the macroscopic determination.

Finally, BEES shows high sensitivity to small fluctuations on SBH values, which is a significant factors for the quest of fabricating nanoscale devices. In particular, the existence

of two barriers appears to be a robust nanoscale feature of the interface, independent of the metal base and the metalization method. Knowledge of these two onsets matters for engineering nanoscopic Ge-based devices, as it will contribute to the response of such miniaturized Schottky diodes. In turn, we demonstrate how the sensitivity of BEES can be used to characterize the interface.

## Acknowledgement

This work has been funded by MAT2017-85089-C2-1-R, MAT2017-88258-R, Maria de Maeztu Programme CEX2018-000805-M (MINECO, Spain), MIUR Progetto Premiale 2012 *EOS: organic electronics for advanced research instrumentation* (Italy), and ERC-2013-SYG-610236 (EU). A portion of this research was carried out at the Jet Propulsion Laboratory (CALTECH) under contract with NASA.

## Supporting Information Available

The supporting information includes X-ray Photoelectron Spectroscopy (S1), X-ray Diffraction (XRD) characterization of the interfaces (S2) and, Atomic Force Microscopy (AFM) on the Ge(100) substrate. A study of the back ohmic contact (S4) and I-V vs T characteristics (S5). Details about the theoretical modelling of interfaces are given in S6. Figures S1 and S2 show XPS spectra. Figures S3 and S6 give  $\theta$ - $2\theta$  scans for Au/Ge(100) and Pt/Ge(100). Figure S4 shows a rocking curve for the Au(220) and Ge(400) peaks and, Figure S5  $\phi$ -scans for G(400), Au(111), Au(200) and Au(220) peaks. Figure S7 depicts an AFM image of the substrate, Ge(100). Figure S8 gives I-V curves for Ohmic back-contact. Figure S9 shows I-V macroscopic characteristics. Figure S10 illustrates the effect of different theoretical thresholds on BEEM ab-initio I-Vs. Figures S11 and S12 are schematic representations for the interfaces M(001)/Ge(001) and M(111)/Ge(001). Figure S13 compares the DOS for two model interfaces, which have been used to get the interface dipoles. Table S1 gives a summary

of different parameters determined from the ab-initio optimization of the model interfaces.

This material is available free of charge via the Internet at <http://pubs.acs.org/>.

## References

- (1) Hu, J.; Wong, H.-S. P.; Saraswat, K. Novel Contact Structures for High Mobility Channel Materials. *MRS Bull.* **2011**, *36*, 112–120.
- (2) Chroneos, A.; Schwingenschlögl, U.; Dimoulas, A. Impurity Diffusion, Point Defect Engineering, and Surface/Interface Passivation in Germanium. *Ann. Phys. (Berlin, Ger.)* **2012**, *524*, 123–132.
- (3) Ponath, P.; Posadas, A. B.; Demkov, A. A. Ge(001) Surface Cleaning Methods for Device Integration. *Appl. Phys. Rev.* **2017**, *4*, 021308.
- (4) Robertson, J.; Wallace, R. M. High-K Materials and Metal Gates for CMOS Applications. *Mat. Sci. Eng., R* **2015**, *88*, 1 – 41.
- (5) Scappucci, G.; Capellini, G.; Klesse, W. M.; Simmons, M. Y. New Avenues to an Old Material: Controlled Nanoscale Doping of Germanium. *Nanoscale* **2013**, *5*, 2600–2615.
- (6) Toriumi, A.; Nishimura, T. Germanium CMOS Potential from Material and Process Perspectives: Be More Positive About Germanium. *Jpn. J. Appl. Phys.* **2018**, *57*, 010101.
- (7) Clarysse, T.; Eyben, P.; Janssens, T.; Hoflijk, I.; Vanhaeren, D.; Satta, A.; Meuris, M.; Vandervorst, W.; Bogdanowicz, J.; Raskin, G. Active Dopant Characterization Methodology for Germanium. *J. Vac. Sci. Technol. B* **2006**, *24*, 381–389.
- (8) Dimoulas, A.; Tsipas, P.; Sotiropoulos, A.; Evangelou, E. K. Fermi-Level Pinning and Charge Neutrality Level in Germanium. *Appl. Phys. Lett.* **2006**, *89*, 252110.

- 1  
2  
3 (9) Kuzum, D.; Martens, K.; Krishnamohan, T.; Saraswat, K. C. Characteristics of Surface  
4 States and Charge Neutrality Level in Ge. *Appl. Phys. Lett.* **2009**, *95*, 252101.  
5  
6  
7  
8 (10) Nishimura, T.; Kita, K.; Toriumi, A. Evidence for Strong Fermi-Level Pinning due to  
9 Metal-Induced Gap States at Metal/Germanium Interface. *Appl. Phys. Lett.* **2007**, *91*,  
10 123123.  
11  
12  
13  
14 (11) Tsipas, P.; Dimoulas, A. Modeling of Negatively Charged States at the Ge Surface and  
15 Interfaces. *Appl. Phys. Lett.* **2009**, *94*, 012114.  
16  
17  
18  
19 (12) Yao, H. B.; Chia, D. Z. Effect of the Inversion Layer on the Electrical Characterization  
20 of Pt Germanide/n-Ge(001) n-Ge(001) Schottky Contacts. *Appl. Phys. Lett.* **2006**, *89*,  
21 242117.  
22  
23  
24  
25  
26 (13) Lee, J.-H.; Lee, E. K.; Joo, W.-J.; Jang, Y.; Kim, B.-S.; Lim, J. Y.; Choi, S.-H.;  
27 Ahn, S. J.; Ahn, J. R.; Park, M.-H.; Yang, C.-W.; Choi, B. L.; Hwang, S.-W.; Whang, D.  
28 Wafer-Scale Growth of Single-Crystal Monolayer Graphene on Reusable Hydrogen-  
29 Terminated Germanium. *Science* **2014**, *344*, 286–289.  
30  
31  
32  
33  
34 (14) Wang, G.; Zhang, M.; Zhu, Y.; Ding, G.; Jiang, D.; Guo, Q.; Liu, S.; Xie, X.; Chu, P. K.;  
35 Di, Z.; Wang, X. Direct Growth of Graphene Film on Germanium Substrate. *Sci. Rep.*  
36 **2013**, *3*, 2465.  
37  
38  
39  
40  
41 (15) Pasternak, I.; Wesolowski, M.; Jozwik, I.; Lukosius, M.; Lupina, G.; Dabrowski, P.;  
42 Baranowski, J. M.; Strupinski, W. Graphene Growth on Ge(100)/Si(100) Substrates  
43 by CVD Method. *Sci. Rep.* **2016**, *6*, 21773.  
44  
45  
46  
47 (16) Loscutoff, P. W.; Bent, S. F. Reactivity of the Germanium Surface: Chemical Passiva-  
48 tion and Functionalization. *Ann. Rev. Phys. Chem.* **2006**, *57*, 467–495.  
49  
50  
51  
52 (17) Scace, R. I.; Slack, G. A. Solubility of Carbon in Silicon and Germanium. *J. Chem.*  
53 *Phys.* **1959**, *30*, 1551–1555.  
54  
55  
56  
57  
58  
59  
60

- 1  
2  
3 (18) Colace, L.; Masini, G.; Galluzzi, F.; Assanto, G.; Capellini, G.; Di Gaspare, L.;  
4 Palange, E.; Evangelisti, F. Metal-Semiconductor-Metal near-Infrared Light Detector  
5 Based on Epitaxial Ge/Si. *Appl. Phys. Lett.* **1998**, *72*, 3175–3177.  
6  
7  
8  
9  
10 (19) Yan, C.; Singh, N.; Cai, H.; Gan, C. L.; Lee, P. S. Network-Enhanced Photoresponse  
11 Time of Ge Nanowire Photodetectors. *ACS Appl. Mater. Interfaces* **2010**, *2*, 1794–1797.  
12  
13  
14 (20) Dushaq, G.; Nayfeh, A.; Rasras, M. Metal-Germanium-Metal Photodetector Grown on  
15 Silicon Using Low Temperature RF-PECVD. *Opt. Express* **2017**, *25*, 32110–32119.  
16  
17  
18  
19 (21) Vivien, L.; Osmond, J.; Fédéli, J.-M.; Marris-Morini, D.; Crozat, P.; Damlencourt, J.-  
20 F.; Cassan, E.; Lecunff, Y.; Laval, S. 42 GHz p.i.n Germanium Photodetector Integrated  
21 in a Silicon-on-Insulator Waveguide. *Opt. Express* **2009**, *17*, 6252–6257.  
22  
23  
24  
25  
26 (22) Cao, L.; Park, J.-S.; Fan, P.; Clemens, B.; Brongersma, M. L. Resonant Germanium  
27 Nanoantenna Photodetectors. *Nano Lett.* **2010**, *10*, 1229–1233.  
28  
29  
30  
31 (23) Sahni, S.; Luo, X.; Liu, J.; hong Xie, Y.; Yablonovitch, E. Junction Field-Effect-  
32 Transistor-Based Germanium Photodetector on Silicon-on-Insulator. *Opt. Lett.* **2008**,  
33 *33*, 1138–1140.  
34  
35  
36  
37 (24) Tung, R. T. The Physics and Chemistry of the Schottky Barrier Height. *Appl. Phys.*  
38 *Rev.* **2014**, *1*, 011304.  
39  
40  
41  
42 (25) Dumas, D. C. S.; Gallacher, K.; Millar, R.; MacLaren, I.; Myronov, M.; Leadley, D. R.;  
43 Paul, D. J. Silver Antimony Ohmic Contacts to Moderately Doped n-type Germanium.  
44 *App. Phys. Lett.* **2014**, *104*, 162101.  
45  
46  
47  
48 (26) Flores, F.; Tejedor, C. On the Formation of Semiconductor Interfaces. *J. Phys. C: Solid*  
49 *State Phys.* **1987**, *20*, 145–175.  
50  
51  
52  
53 (27) Mönch, W. Barrier Heights of Real Schottky Contacts Explained by Metal-Induced  
54 Gap States and Lateral Inhomogeneities. *J. Vac. Sci. Technol. B* **1999**, *17*, 1867–1876.  
55  
56  
57  
58  
59  
60

- 1  
2  
3 (28) Sasaki, S.; Nakayama, T. Defect Distribution and Schottky Barrier at Metal/Ge Inter-  
4 faces: Role of Metal-Induced Gap States. *Jpn. J. Appl. Phys.* **2016**, *55*, 111302.  
5  
6  
7  
8 (29) Bell, L. D. Ballistic Electron Emission Microscopy and Spectroscopy: Recent Results  
9 and Related Techniques. *J. Vac. Sci. Technol. B* **2016**, *34*, 040801.  
10  
11  
12 (30) Buzio, R.; Gerbi, A.; Marrè, D.; Barra, M.; Cassinese, A. Electron Injection Barrier  
13 and Energy-Level Alignment at the Au/PDI8-CN2 Interface via Current-Voltage Mea-  
14 surements and Ballistic Emission Microscopy. *Org. Electron.* **2015**, *18*, 44 – 52.  
15  
16  
17  
18 (31) von Känel, H.; Meyer, T.; Klemenc, M. Microscopy and Spectroscopy of Buried Nanos-  
19 tructures. *J. Electron Spectrosc. Relat. Phenom.* **2000**, *109*, 197 – 209.  
20  
21  
22  
23 (32) Bell, L. D.; Milliken, A. M.; Manion, S. J.; Kaiser, W. J.; Fathauer, R. W.; Pike, W. T.  
24 Ballistic-Electron-Emission Microscopy of Strained Si<sub>1-x</sub>Ge<sub>x</sub> Layers. *Phys. Rev. B*  
25 **1994**, *50*, 8082–8085.  
26  
27  
28  
29 (33) Gerbi, A.; González, C.; Buzio, R.; Manca, N.; Marrè, D.; Bell, L. D.; Trabada, D. G.;  
30 Di Matteo, S.; de Andres, P. L.; Flores, F. Accurate *ab-initio* Determination of Bal-  
31 listic Electron Emission Spectroscopy: Application to Au/Ge. *Phys. Rev. B* **2018**, *98*,  
32 205416.  
33  
34  
35  
36  
37  
38  
39 (34) Deegan, T.; Hughes, G. An X-ray Photoelectron Spectroscopy Study of the HF Etching  
40 of Native Oxides on Ge(111) and Ge(100) Surfaces. *Appl. Surf. Sci.* **1998**, *123-124*, 66  
41 – 70.  
42  
43  
44  
45  
46 (35) Bodlaki, D.; Yamamoto, H.; Waldeck, D.; Borguet, E. Ambient Stability of Chemically  
47 Passivated Germanium Interfaces. *Surf. Sci.* **2003**, *543*, 63 – 74.  
48  
49  
50  
51 (36) Buriak, J. M. Organometallic Chemistry on Silicon and Germanium Surfaces. *Chem.*  
52 *Rev.* **2002**, *102*, 1271–1308.  
53  
54  
55  
56  
57  
58  
59  
60

- 1  
2  
3 (37) Choi, K.; Buriak, J. M. Hydrogermylation of Alkenes and Alkynes on Hydride-  
4 Terminated Ge(100) Surfaces. *Langmuir* **2000**, *16*, 7737–7741.  
5  
6  
7  
8 (38) Sze, S. M.; Kwok, K. N. *Physics of Semiconductor Devices*; John Wiley and Sons, 2006.  
9  
10  
11 (39) Weisstein, E. W. Polylogarithm. MathWorld – A Wolfram Web Resource, 2018;  
12 <http://mathworld.wolfram.com/Polylogarithm.html>.  
13  
14  
15 (40) Bell, L. D.; Kaiser, W. J. Observation of Interface Band Structure by Ballistic-Electron-  
16 Emission Microscopy. *Phys. Rev. Lett.* **1988**, *61*, 2368–2371.  
17  
18  
19 (41) Prietsch, M.; Ludeke, R. Ballistic-Electron-Emission Microscopy and Spectroscopy of  
20 GaP(110)-Metal Interfaces. *Phys. Rev. Lett.* **1991**, *66*, 2511–2514.  
21  
22  
23  
24 (42) Prietsch, M. Ballistic-Electron Emission Microscopy (BEEM): Studies of  
25 Metal/Semiconductor Interfaces with Nanometer Resolution. *Phys. Rep.* **1995**,  
26 *253*, 163 – 233.  
27  
28  
29 (43) Lewis, J.; Jelinek, P.; Ortega, J.; Demkov, A. A.; Trabada, D. G.; Haycock, B.;  
30 Wang, H.; Adams, G.; Tomfohr, J. K.; Abad, E.; Wang, H.; Drabold, D. A. Advances  
31 and Applications in the FIREBALL *ab-initio* Tight-Binding Molecular-Dynamics For-  
32 malism. *Phys. Status Solidi B* **2011**, *248*, 1989.  
33  
34  
35 (44) Fisher, D.; Lee, P. Relation Between Conductivity and Transmission Matrix. *Phys. Rev.*  
36 *B* **1981**, *23*, 6851–6854.  
37  
38  
39 (45) Claveau, Y.; Matteo, S. D.; de Andres, P. L.; Flores, F. Electron Transport in Ultra-  
40 Thin Films and Ballistic Electron Emission Microscopy. *J. Phys.: Condens. Matter*  
41 **2017**, *29*, 115001.  
42  
43  
44 (46) Ladstädter, F.; de Pablos, P. F.; Hohenester, U.; Puschnig, P.; Ambrosch-Draxl, C.;  
45 de Andres, P. L.; Garcia-Vidal, F. J.; Flores, F. Hot-Electron Lifetimes in Metals: A  
46  
47  
48  
49  
50  
51  
52  
53  
54  
55  
56  
57  
58  
59  
60

- 1  
2  
3 combined ab-initio calculation and Ballistic Electron Emission Spectroscopy analysis.  
4  
5 *Phys. Rev. B* **2003**, *68*, 085107.  
6  
7
- 8 (47) de Andres, P. L.; Garcia-Vidal, F. J.; Reuter, K.; Flores, F. Theory of Ballistic Electron  
9 Emission Microscopy. *Prog. Surf. Sci.* **2001**, *66*, 3 – 51.  
10  
11
- 12 (48) Bell, L. D.; Kaiser, W. J. Observation of Interface Band Structure by Ballistic-Electron-  
13 Emission Microscopy. *Phys. Rev. Lett.* **1988**, *61*, 2368–2371.  
14  
15
- 16 (49) Zwerdling, S.; Lax, B.; Roth, L. M.; Button, K. J. Exciton and Magneto-Absorption of  
17 the Direct and Indirect Transitions in Germanium. *Phys. Rev.* **1959**, *114*, 80–89.  
18  
19
- 20 (50) Nicholls, J. M.; Hansson, G. V.; Karlsson, U. O.; Persson, P. E. S.; Uhrberg, R. I. G.;  
21 Engelhardt, R.; Flodström, S. A.; Koch, E.-E. Bulk Electronic Structure of Germanium  
22 studied with Angle-resolved Photoemission. *Phys. Rev. B* **1985**, *32*, 6663–6674.  
23  
24  
25  
26  
27
- 28 (51) Jancu, J.-M.; Scholz, R.; Beltram, F.; Bassani, F. Empirical spds\* Tight-Binding cal-  
29 culation for Cubic Semiconductors: General Method and Material Parameters. *Phys.*  
30 *Rev. B* **1998**, *57*, 6493–6507.  
31  
32  
33  
34  
35
- 36 (52) Weismann, A.; Wenderoth, M.; Lounis, S.; Zahn, P.; Quass, N.; Ulbrich, R. G.; Ded-  
37 erichs, P. H.; Blügel, S. Seeing the Fermi Surface in Real Space by Nanoscale Electron  
38 Focusing. *Science* **2009**, *323*, 1190–1193.  
39  
40  
41  
42  
43  
44  
45  
46  
47  
48  
49  
50  
51  
52  
53  
54  
55  
56  
57  
58  
59  
60



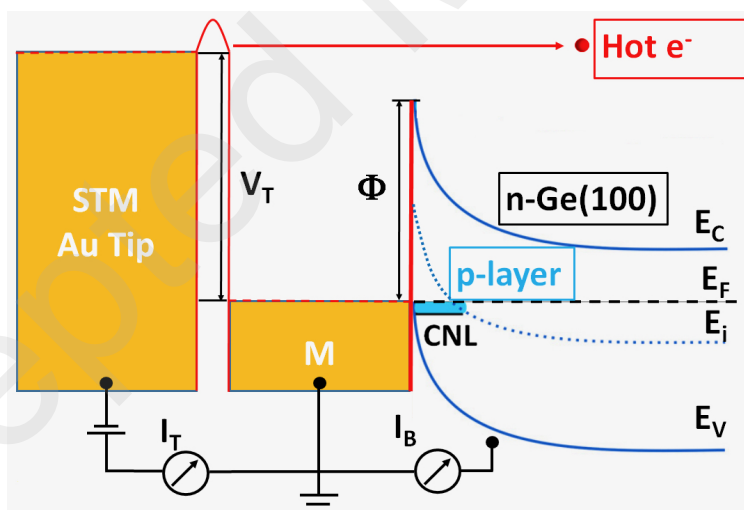
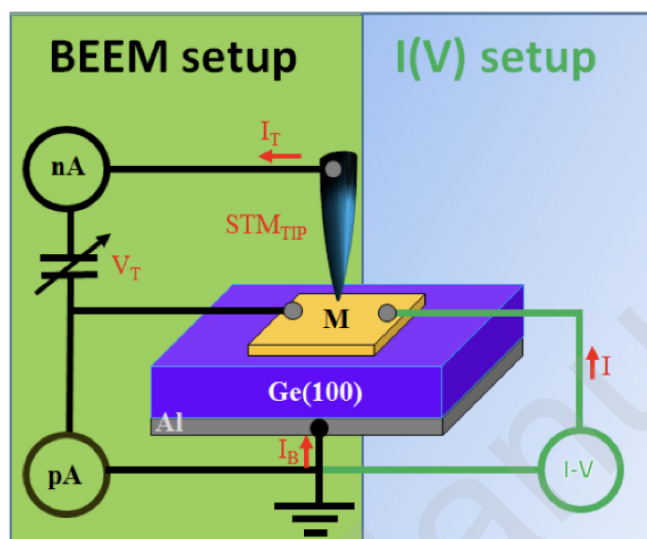


Figure 1: Upper panel: Schematic diagram of the metal/Ge(100) junctions and the experimental setup for BEEM measurements,  $I_B(V)$ , acquired under dark at 80 K.  $I_T(V)$  corresponds to the injected current of tunneling electrons. Lower panel: Schematic diagram for energy bands at the junction.

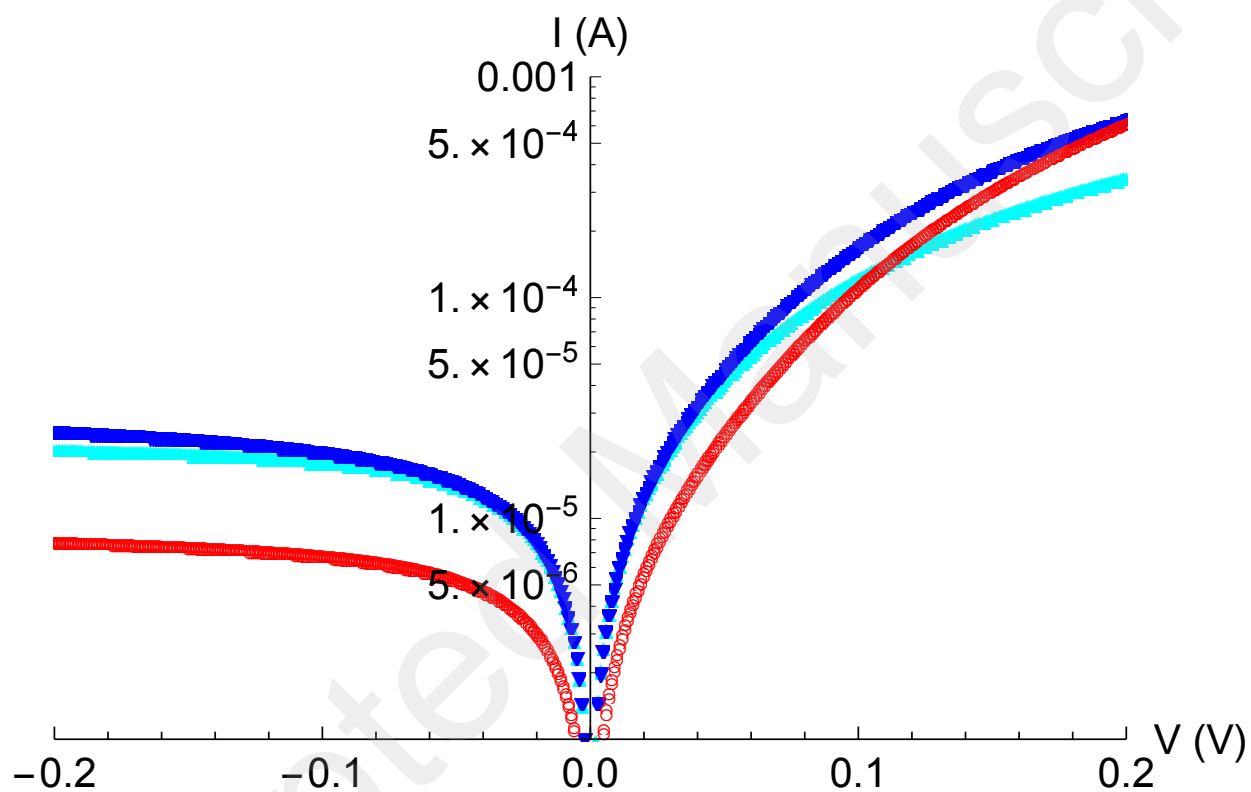


Figure 2: I-V macroscopic characteristics at  $T = 290$  K for the prepared metal/Ge diodes: Au-PVD (cyan), Au-PLD (blue), Pt-PLD (red). Values for the Schottky-barrier ( $\Phi$ ) and ideality factor ( $n$ ) computed using TE theory for  $V > \frac{3kT}{q}$  are given in Table 1.

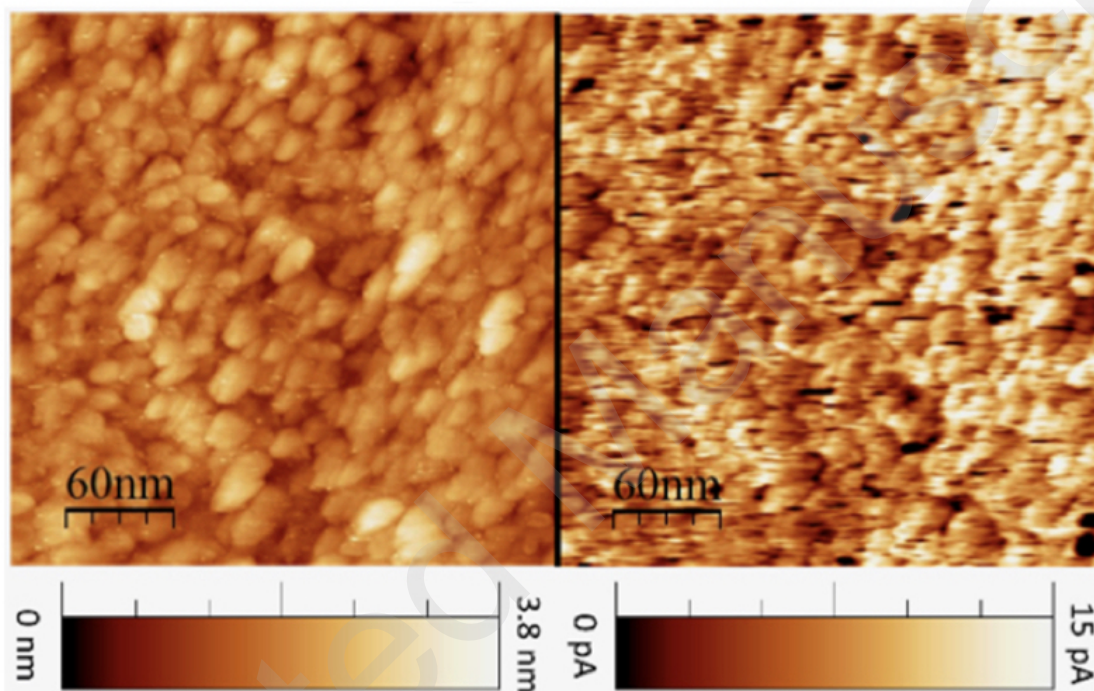


Figure 3: Representative images for topography and the related BEEM current map acquired over a representative region ( $300 \times 300 \text{ nm}^2$ ) of the Au electrode at 80 K.

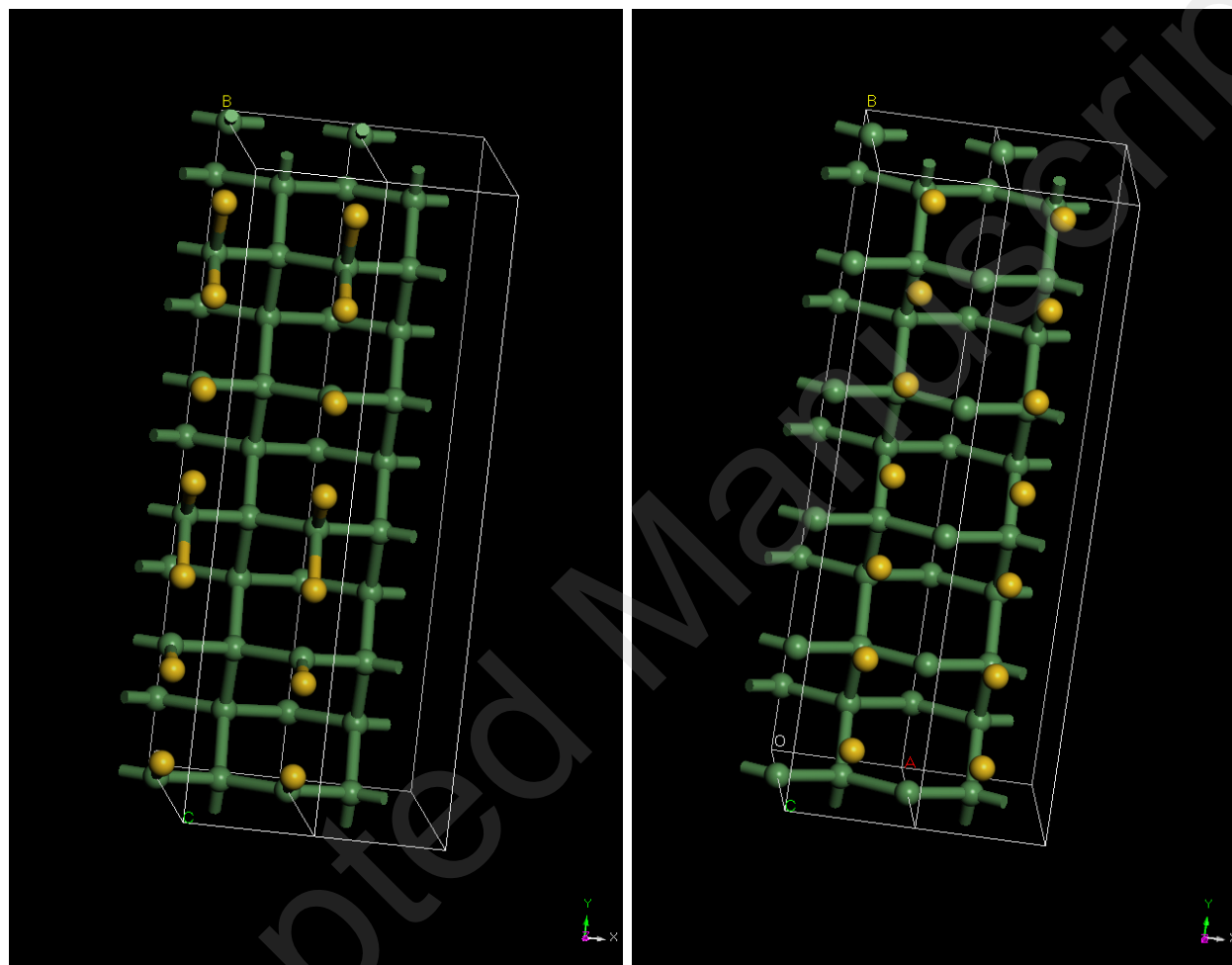


Figure 4:  $1 \times 7$  Au(011)/ $1 \times 5$  Ge(001) interface. Left panel: atop and quasi-bridges (labeled T in the text). Right panel: registry obtained by a displacement  $\frac{1}{2}\vec{v}_1$  where atoms adsorb near mostly bridges (labeled B in the text). For the sake of clarity, only a few layers at the interface are shown, actual calculations include enough layers to give a converged result, cf. Supplementary Information.

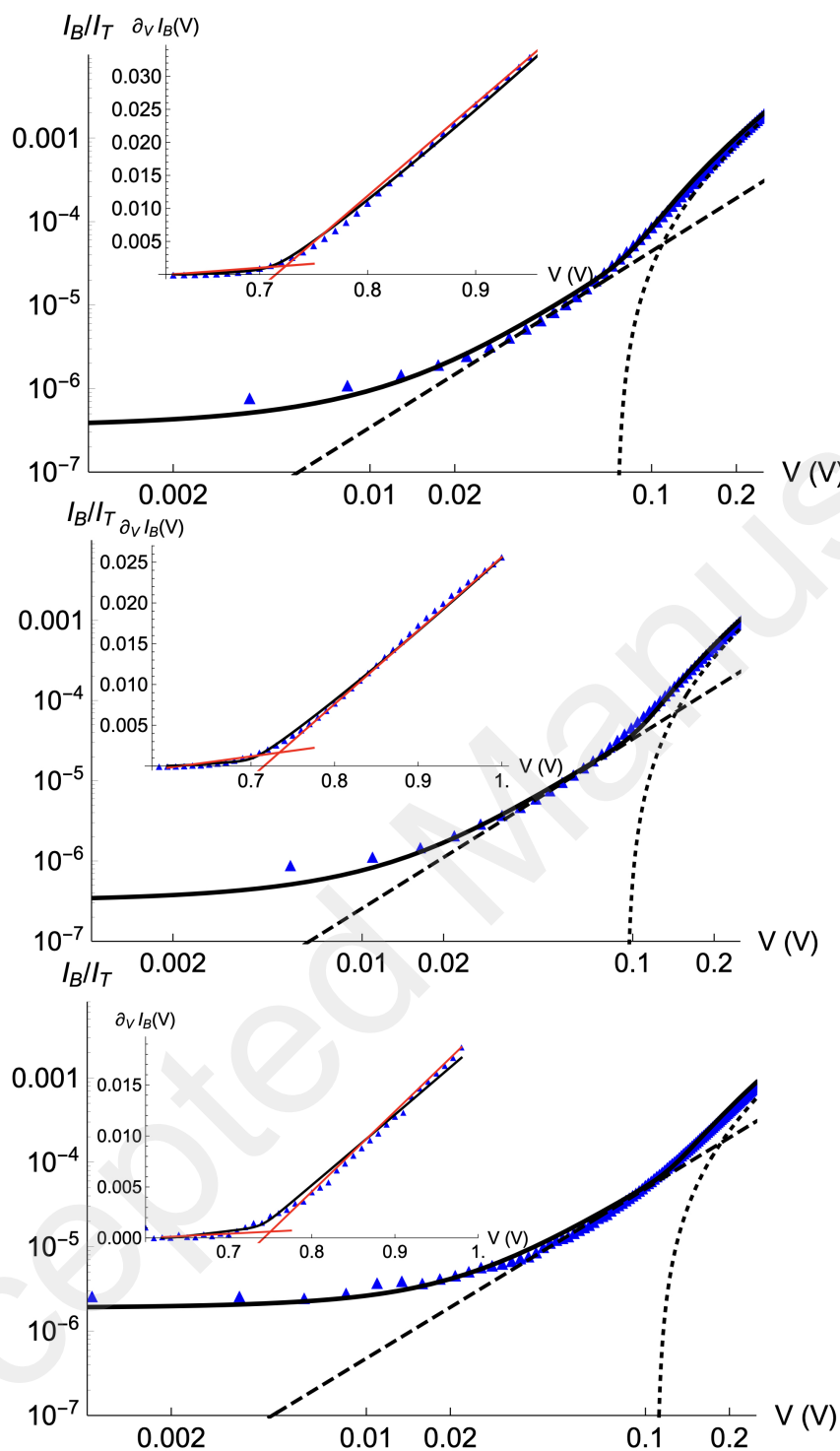


Figure 5: Experimental BEES data (blue triangles,  $T = 80$  K) for the three cases in Table 1: top panel (Au-PLD,  $I_T = 2.5$  nA), middle panel (Au-PVD,  $I_T = 2$  nA), lower panel (Pt-PLD,  $I_T = 3$  nA). The origin of each Log-Log plot corresponds to the lowest barrier for each case, cf. Table 1. Black thick line: best fit from Equation (3) at  $T = 80$  K. Black dashed and dotted lines give the individual contributions of each barrier at  $T = 0$  K ( $I = \alpha V_T^\mu$ , with  $\mu$  derived from an ab-initio calculation, cf. Table 1. Inset: a comparison of derivatives for experimental data and best fits (black line).

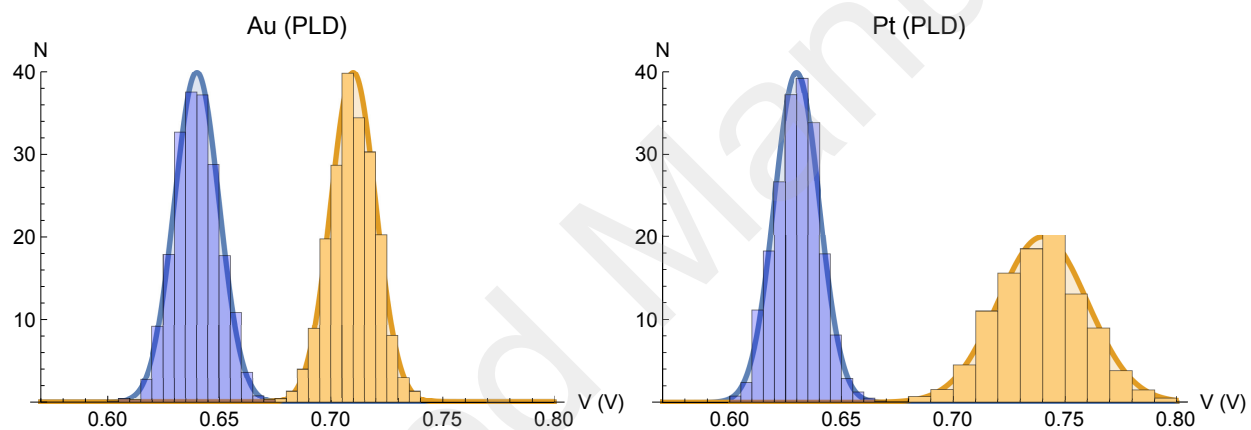


Figure 6: Schottky-barrier probability distributions for Au (PLD) and Pt (PLD).

Table 1: Energies in eV. Left: Schottky barrier ( $\Phi$ ) and ideality factor ( $n$ ) best-fit determination using macroscopic TE, cf. Figure 2. Right: Schottky barrier determination ( $\Phi_{1,2}$ ) using the ab-initio ballistic phase-space model, cf. Fig. 5. Coefficients  $\alpha_2$  and  $\alpha_1$  are proportional to the contribution of each onset  $\Phi_2$  and  $\Phi_1$  to the BEEM current.  $\mu$  gives the effective phase-space volumen, derived from ab-initio calculations (see text). The figure of merit,  $R = \frac{1}{N} \sum_1^N | \log_{10} I_E - \log_{10} I_M |$ , has been computed in the interval ( $V_{T_1}, V_{T_2}$ ) comparing the model intensities,  $I_M$ , to the experimental ones,  $I_E$ .

SAMPLE	$\Phi$	$n$	$\Phi_1$	$\alpha_1$	$\Phi_2$	$\alpha_2$	$\mu$	R	$V_{T_1}$	$V_{T_2}$
Au (PVD)	0.61	1.03	0.605	1	0.700	9	2.11	0.096	0.577	1.072
Au (PLD)	0.62	1.03	0.637	1	0.710	11	2.11	0.095	0.607	1.000
Pt (PLD)	0.63	1.14	0.630	1	0.740	6	2.01	0.031	0.604	0.982

## Graphical TOC Entry

